PHYSICAL REVIEW X **10,** 041023 (2020)

Single-Particle Spectral Function Formulated and Calculated by Variational Monte Carlo Method with Application to *d*-Wave Superconducting State

Maxime Charlebois[1,2,3,4,*] and Masatoshi Imada[1,4,5]

[1]*Waseda Research Institute for Science and Engineering, Waseda University,*
3-4-1, Okubo, Shinjuku, Tokyo 169-8555, Japan
[2]*Center for Computational Quantum Physics, Flatiron Institute,*
162 Fifth Avenue, New York, New York 10010, USA
[3]*Département de Chimie, Biochimie et Physique, Institut de Recherche sur l'Hydrogène, Université du Québec à Trois-Rivières, Trois-Rivières, Québec G9A 5H7, Canada*
[4]*Department of Applied Physics, The University of Tokyo, Hongo, Bunkyo-ku, Tokyo 113-8656, Japan*
[5]*Toyota Physical and Chemical Research Institute, 41-1, Yokomichi, Nagakute, Aichi 480-1118, Japan*

(Received 20 December 2019; revised 29 July 2020; accepted 14 September 2020; published 2 November 2020)

A method to calculate the one-body Green's function for ground states of correlated electron materials is formulated by extending the variational Monte Carlo method. We benchmark against the exact diagonalization (ED) for the one- and two-dimensional Hubbard models of 16-site lattices, which proves high accuracy of the method. The application of the method to a larger-sized Hubbard model on the square lattice correctly reproduces the Mott insulating behavior at half-filling and gap structures of the *d*-wave superconducting state of the hole-doped Hubbard model in the ground state optimized by enforcing the charge uniformity, evidencing a wide applicability to strongly correlated electron systems. From the obtained *d*-wave superconducting gap of the charge-uniform state, we find that the gap amplitude at the antinodal point is several times larger than the experimental value when we employ a realistic parameter as a model of the cuprate superconductors. The effective attractive interaction of carriers in the *d*-wave superconducting state inferred for an optimized state of the Hubbard model is as large as the order of the nearest-neighbor transfer, which is far beyond the former expectation in the cuprates. We discuss the nature of the superconducting state of the Hubbard model in terms of the overestimate of the gap and the attractive interaction in comparison to the cuprates.

DOI: 10.1103/PhysRevX.10.041023

Subject Areas: Computational Physics,
Condensed Matter Physics,
Strongly Correlated Materials

I. INTRODUCTION

Dynamical properties often provide us with crucial insights into open issues of strongly correlated electron systems. In particular, the momentum- and energy-resolved single-particle spectral function $A(\mathbf{k},\omega)$, which is proportional to the imaginary part of the Green's function $G(\mathbf{k},\omega)$ with the momentum $\mathbf{k}$ and the frequency ω, helps us understand how an electron moves in an environment of other mutually interacting electrons and provides us with properties of the excited states, which in turn reveal the equilibrium properties as well.

The copper-oxide high-T_c superconductors' spectral function $A(\mathbf{k},\omega)$ has been extensively studied by angle-resolved photoemission spectroscopy (ARPES), which has greatly contributed to elucidate the properties of superconducting as well as anomalous normal metallic properties, including the pseudogap, Fermi arc, and d-wave superconducting gap structure itself [1,2].

Numerical methods to clarify the dynamics of the strongly correlated electron systems have been hampered by various difficulties such as the fermion sign problem [3–6] in quantum Monte Carlo methods, and intrinsic quantum entanglement of electrons at long distances. Nevertheless, linear response quantities such as the spin and charge dynamical structure factors—$S(\mathbf{k},\omega)$ and $N(\mathbf{k},\omega)$, respectively—defined below have been studied by limited methods such as the exact diagonalization (ED) [7,8] and time-dependent density matrix renormalization group [9,10]. However, these methods have their own limitations; namely, they are amenable only in small system sizes and in one-dimensional lattice structures, respectively.

---

[*] maxime.charlebois@uqtr.ca

In addition to the exact diagonalization, $G(\mathbf{k},\omega)$ has been studied by the cluster extension of the dynamical mean-field theory (cDMFT) [11–13], but the allowed momentum resolution is severely limited by the cluster size, usually smaller than 10 electronic sites. The cDMFT method is generally combined with a periodization procedure in order to restore translation invariance, and it provides the data at interpolated momenta $\mathbf{k}$ [14–17]. However, we need to be cautious about these periodizations, and the results should be regarded as estimators because the momentum resolution is limited by the cluster size. This case is true even for inhomogeneous extension of cDMFT [18,19], where the large supercluster still retains the self-energy modulation of the original smallest cluster [20]. The need to study bigger clusters remains.

The recent formulation of the time-dependent variational Monte Carlo method based on the variational principle opened a way to study the long-time dynamics [21,22], but it has not been extensively applied yet to interacting fermion systems except for in a few examples [23]. Meanwhile, methods of calculating the spin and charge dynamical structure factors utilizing the variational wave functions for ground and excited states have been proposed recently [24–28]. Some attempts have been made to calculate the excitation spectrum on larger clusters of the t-J model [29,30].

Here, we formulate a method of calculating the Green's function $G(\mathbf{k},\omega)$ and the spectral function $A(\mathbf{k},\omega) = -(1/\pi)\mathrm{Im}G(\mathbf{k},\omega)$ and show its accuracy by comparing with the exact results. It reproduces the feature of the spin-charge separation and excitation continuum in the one-dimensional Hubbard model.

The method is applied to the Hubbard model on the square lattice as well. In the optimized d-wave superconducting solution, though it is an excited state in the competition with the stripe states [31–33], the d-wave symmetry of the gap structure is correctly reproduced in the spectral function in this charge-uniform lowest-energy state. However, the gap amplitude is several times larger than the size in the experimentally observed gap of the cuprate superconductors, if we employ a widely accepted parameter mapping. The effective attractive interaction of carriers in this state is then estimated again to be extremely large, on the order of or even larger than the nearest-neighbor transfer energy t in the Hubbard model. We discuss implications of the results.

Finally, in the Supplemental Material [34], the reader can access the fully functional open-source code that was used to generate the data. The code is an extension based on the open-source code mVMC [35].

II. METHOD

A. Green's function

Here, we present a very general scheme to estimate the one-body Green's function from the Lehman representation:

$$G_\sigma(\mathbf{k},\omega) = G^h_\sigma(\mathbf{k},\omega) + G^e_\sigma(\mathbf{k},\omega), \tag{1}$$

$$G^h_\sigma(\mathbf{k},\omega) = \langle\Omega|\hat{c}^\dagger_{\mathbf{k}\sigma}\frac{1}{\omega + i\eta - \Omega + \hat{H}}\hat{c}_{\mathbf{k}\sigma}|\Omega\rangle, \tag{2}$$

$$G^e_\sigma(\mathbf{k},\omega) = \langle\Omega|\hat{c}_{\mathbf{k}\sigma}\frac{1}{\omega + i\eta + \Omega - \hat{H}}\hat{c}^\dagger_{\mathbf{k}\sigma}|\Omega\rangle. \tag{3}$$

Note that $\hat{c}_{\mathbf{k}\sigma}$ ($\hat{c}^\dagger_{\mathbf{k}\sigma}$) annihilates (creates) an electron of momentum $\mathbf{k}$ and spin σ. This approach requires knowledge of the ground state $|\Omega\rangle$ of a Hamiltonian $\hat{H}$ with energy Ω. The "hat" notation is used here to represent an operator as opposed to any matrix representation. Note that η is a small real number, a Lorentzian broadening factor.

The Lehman representation can be evaluated explicitly with ED since we have a complete and exact representation of the Hamiltonian eigenstates, but this technique is limited to small clusters. To evaluate the Green's function for the cases not amenable to the exact diagonalization, we can use a method similar to the approach used to calculate the spin and charge dynamical structure factors by exhausting an important subspace of the Hilbert space for the excitations [24–28]. In this framework, the time evolutions by the Hamiltonian in the $N-1$ particle sector for $G^h_\sigma(\mathbf{k},\omega)$ [Eq. (2)] and $N+1$ particle sector for $G^e_\sigma(\mathbf{k},\omega)$ [Eq. (2)] are treated within such an important subspace.

Then, the idea of the present method is to restrict the Hilbert space of the one-particle or hole-excited sector of the Hamiltonian to a set of vectors:

$$|h_{\mathbf{k}n}\rangle = \hat{A}_n\hat{c}_{\mathbf{k}}\hat{B}_n|\Omega\rangle \quad \text{for hole excitations,} \tag{4}$$

$$|e_{\mathbf{k}n}\rangle = \hat{A}^\dagger_n\hat{c}^\dagger_{\mathbf{k}}\hat{B}^\dagger_n|\Omega\rangle \quad \text{for electron excitations,} \tag{5}$$

where $\hat{A}_n$ and $\hat{B}_n$ are operators that together conserve the number of electrons N_e and momentum $\mathbf{k}$. Here, $|\Omega\rangle$ is an approximate ground state of the N particle sector obtained by our variational Monte Carlo method for the ground state, and $|h_{\mathbf{k}n}\rangle$ and $|e_{\mathbf{k}n}\rangle$ belong to the $N-1$ and $N+1$ particle sectors, respectively. Note that for the Krylov basis of excitation, used in ED, $\hat{B}_n = \hat{I}$ and $\hat{A}_n = \hat{H}^n$, where n is the number of band Lanczos iterations. Usually in ED, at every iteration of the band Lanczos method, the excited-state basis is orthogonalized to every other excitation. But it is possible, and sometimes more convenient, to work in the nonorthogonal basis.

B. Nonorthogonal basis for excited states

Now, we construct the basis to represent the excited states $|h_{\mathbf{k}n}\rangle$ and $|e_{\mathbf{k}n}\rangle$. The excited states employed in the method introduced below are not necessarily orthogonal to one another. Although these excitations are not orthogonal, we can use tools to generate a spectrum with eigenstates that are orthogonal. For this purpose, we need to introduce a number of overlap matrices:

$$O^h_{\mathbf{k},mn} = \langle h_{\mathbf{k}m}|\hat{I}|h_{\mathbf{k}n}\rangle, \qquad O^e_{\mathbf{k},mn} = \langle e_{\mathbf{k}m}|\hat{I}|e_{\mathbf{k}n}\rangle, \tag{6}$$

where $\hat{I}$ is the identity operator and the matrix notation is expressed with the indices m and n. It is important to distinguish the operator notation (with a "hat" here) from the matrix notation since they are different in a nonorthogonal basis. Indeed, the matrices $O_{\mathbf{k},mn}$ are representations of the identity operator in this nonorthogonal basis.

Using the same basis, we evaluate the effective Hamiltonian matrices:

$$H^h_{\mathbf{k},mn} = \langle h_{\mathbf{k}m}|\hat{H}|h_{\mathbf{k}n}\rangle, \qquad H^e_{\mathbf{k},mn} = \langle e_{\mathbf{k}m}|\hat{H}|e_{\mathbf{k}n}\rangle. \tag{7}$$

In general, the basis set on the restricted Hilbert subspace is nonorthogonal, and thus we need to solve the generalized eigenvalue problem [36] within this subspace as

$$\mathbf{H}_\mathbf{k}|E_{\mathbf{k}l}\rangle = E_{\mathbf{k}l}\mathbf{O}_\mathbf{k}|E_{\mathbf{k}l}\rangle, \tag{8}$$

where $\mathbf{H}_\mathbf{k}$ and $\mathbf{O}_\mathbf{k}$ are matrices whose (m, n) components are given in Eqs. (7) and (6), respectively, in the basis of $|h_{\mathbf{k}n}\rangle$ or $|e_{\mathbf{k}n}\rangle$. The solution of this generalized eigenvalue problem is represented by the lth eigenvalue $E_{\mathbf{k}l}$ and the corresponding eigenstate coefficients of its eigenvector $|E_{\mathbf{k}l}\rangle$ represented in the basis of $|h_{\mathbf{k}n}\rangle$ or $|e_{\mathbf{k}n}\rangle$, where we express them as $|E^h_{\mathbf{k}l}\rangle$ and $|E^e_{\mathbf{k}l}\rangle$, respectively, and describe them as $|E_{\mathbf{k}l}\rangle$, inclusively. Now, we have an orthogonal basis of eigenstates of the Hamiltonian. The orthogonality of the eigenvector $|E_{\mathbf{k}l}\rangle$ is represented by $\langle E_{\mathbf{k}l}|\mathbf{O}_\mathbf{k}|E_{\mathbf{k}j}\rangle = \delta_{lj}$. The eigenvectors expand the basis of the subspace defined by the restricted Hilbert space determined by the choice of nonorthogonal excitations. We can insert the complete set of this subspace $\sum_l |E_{\mathbf{k}l}\rangle\langle E_{\mathbf{k}l}|$ in both Eqs. (2) and (3) to obtain

$$G^h_\sigma(\mathbf{k},\omega) = \sum_l \frac{\langle\Omega|\hat{c}^\dagger_{\mathbf{k}\sigma}|E^h_{\mathbf{k}l}\rangle\langle E^h_{\mathbf{k}l}|\hat{c}_{\mathbf{k}\sigma}|\Omega\rangle}{\omega + i\eta - \Omega + E^h_{\mathbf{k}l}}, \tag{9}$$

$$G^e_\sigma(\mathbf{k},\omega) = \sum_l \frac{\langle\Omega|\hat{c}_{\mathbf{k}\sigma}|E^e_{\mathbf{k}l}\rangle\langle E^e_{\mathbf{k}l}|\hat{c}^\dagger_{\mathbf{k}\sigma}|\Omega\rangle}{\omega + i\eta + \Omega - E^e_{\mathbf{k}l}}. \tag{10}$$

Note that $|E^e_{\mathbf{k}l}\rangle$ ($|E^h_{\mathbf{k}l}\rangle$) is the state in the $N+1$ ($N-1$) particle sector with momentum $\mathbf{k}$. It is important to keep in mind that this is an approximation to the Green's function, as we restricted the $N+1$ or $N-1$ particle sector by a variational form defined below, in addition to the approximation to the ground state. By increasing the dimension of the excited subspace, we are able to systematically improve the representation of the excited states toward the exact one represented by the full Hilbert space. The accuracy can be estimated by looking at the convergence of the solution as we increase the number of variational states [37].

This formalism is general, but in this article, we want to apply it to obtain the spectral function of the strongly correlated fermion systems by combining with the variational Monte Carlo (VMC) method. An alternative derivation of Eqs. (9) and (10) can be found in the Appendix A. This derivation is the one implemented in the software provided in the Supplemental Material [34].

C. VMC for the ground state

In the variational Monte Carlo method, we postulate an ansatz, a variational state $|\psi\rangle$ that can be used to calculate the physical quantities associated with that state. To find a good approximation to the ground state, we optimize the variational state in order to minimize the energy measured [35,38].

The measurement of any operator $\hat{A}$ can be done as

$$\langle\hat{A}\rangle = \frac{\langle\psi|\hat{A}|\psi\rangle}{\langle\psi|\psi\rangle} = \sum_x \frac{\langle\psi|\hat{A}|x\rangle\langle x|\psi\rangle}{\langle\psi|\psi\rangle} \tag{11}$$

$$= \sum_x \rho(x)\frac{\langle\psi|\hat{A}|x\rangle}{\langle\psi|x\rangle}, \quad \text{where } \rho(x) = \frac{|\langle x|\psi\rangle|^2}{\langle\psi|\psi\rangle}. \tag{12}$$

In this equation, the sum $\sum_x |x\rangle\langle x|$ is a complete set of every possible electronic configuration in the system. For large systems, however, it becomes computationally unfeasible to sum every configuration. Nevertheless, we can still estimate this sum using a Monte Carlo sampling. The real-space configurations $\{x_\mathbf{s}\}$ are generated with the probability $\rho(x_\mathbf{s})$. Then,

$$\langle\hat{A}\rangle \sim \frac{1}{N_\mathrm{MC}}\sum_{x_\mathbf{s}} \frac{\langle\psi|\hat{A}|x_\mathbf{s}\rangle}{\langle\psi|x_\mathbf{s}\rangle}, \tag{13}$$

where N_MC is the number of Monte Carlo samplings for the summation over $x_\mathbf{s}$, where $\mathbf{s}$ is the index to specify the particle configuration in the real space.

For the ground-state wave function, we employ the variational state:

$$|\psi\rangle = \mathcal{P}_\mathcal{G}\mathcal{P}_\mathcal{J}|\phi\rangle, \tag{14}$$

$$|\phi\rangle = \left(\sum_{i,j} f_{ij}\hat{c}^\dagger_{i\uparrow}\hat{c}^\dagger_{j\downarrow}\right)^{N_e/2}|0\rangle, \tag{15}$$

$$\mathcal{P}_\mathcal{G} = \exp\left(\sum_i g_i\hat{n}_{i\uparrow}\hat{n}_{i\downarrow}\right), \tag{16}$$

$$\mathcal{P}_\mathcal{J} = \exp\left(\sum_{i\neq j} v_{ij}\hat{n}_i\hat{n}_j\right), \tag{17}$$

where the variational parameters are f_{ij}, g_i, and v_{ij}. We define the variational ground state $|\Omega\rangle$ as the state $|\psi\rangle$ that minimizes the variational energy $E = \langle\psi|\hat{H}|\psi\rangle/\langle\psi|\psi\rangle$. To simultaneously optimize the variational parameters, the natural gradient method is applied [39,40]. The resulting ground state $|\Omega\rangle$ and ground-state energy Ω are both deduced from traditional VMC.

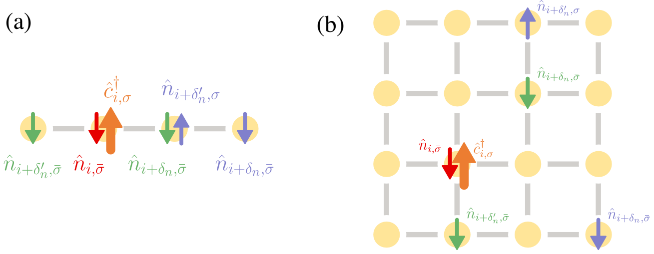

FIG. 1. Geometries of the system studied in this paper. (a) One-dimensional lattice. (b) Two-dimensional square lattice. The excitation on site i is correlated with the presence of electrons on neighboring sites. The charge of the excitation of type $\hat{c}^\dagger_{i\sigma}\hat{n}_{i\bar{\sigma}}|\Omega\rangle$ is represented by the red arrow. The charges of the excitation of type $\hat{c}^\dagger_{i\sigma}\hat{n}_{i+\delta_n,\bar{\sigma}}\hat{n}_{i+\delta'_n,\sigma}|\Omega\rangle$ are represented by the two blue arrows, and the charges of the excitation of type $\hat{c}^\dagger_{i\sigma}\hat{n}_{i+\delta_n,\bar{\sigma}}\hat{n}_{i+\delta'_n,\sigma}|\Omega\rangle$ are represented by the two green arrows. Here, δ_n and δ'_n denote only the difference in position relative to the site i, only for the excitation illustrated here. If we consider the excitation $n+1$, for example, the values δ_n and δ'_n would be different, leading to another "arrow couple" (for green and blue "arrow couples"). We only show one example of such excitation per excitation type, for clarity.

D. Dynamical VMC

Using our knowledge of the ground state calculated from VMC, we can now proceed to calculate the excitation spectrum using the Green's function formalism developed in Sec. II A. The VMC formalism presented in Sec. II C, namely, Eq. (13), can be used not only to calculate the ground state but also to sample the matrices in Eqs. (6) and (7). From these matrices, it is possible to calculate the Green's function using Eqs. (8)–(10).

It is hard to generate excited states that reproduce the Krylov basis since the calculation of $\hat{H}^n$ is very expensive for $n > 1$, as every hopping of electron terms in the Hamiltonian produces a new Pfaffian evaluation. Instead of $\hat{A}_n = H^n$ and $\hat{B}_n = \hat{I}$, which would produce the Krylov basis, we choose a basis where $\hat{A}_n = \hat{I}$ and $\hat{B}_n$ is a combination of different charge excitations $\hat{n}_{i\sigma}$ [28]. To be more explicit, the excitation basis we choose in the expressions of Eqs. (4) and (5) is $|h_{i\sigma n}\rangle = \hat{c}_{i\sigma}|\psi_{\text{in}}\rangle$ and $|e_{i\sigma n}\rangle = \hat{c}^\dagger_{i\sigma}|\psi_{\text{in}}\rangle$, where we introduce

$$|\psi_{\text{in}}\rangle = \{|\Omega\rangle, \hat{n}_{i\bar{\sigma}}|\Omega\rangle, \hat{n}_{i+\delta_n,\bar{\sigma}}\hat{n}_{i+\delta'_n,\sigma}|\Omega\rangle, \hat{n}_{i+\delta_n,\bar{\sigma}}\hat{n}_{i+\delta'_n,\bar{\sigma}}|\Omega\rangle\}. \tag{18}$$

Here, δ_n and δ'_n are a combination of different neighbors to site i for each n. This choice is based on the physical intuition where the creation of an electron on site i is influenced by the presence of electrons with both same and opposite spins on sites $i+\delta$ and $i+\delta'$, respectively. This case is illustrated in Fig. 1 for the two geometries studied in this article. Generally, we consider only excitations within a certain range $\delta = (\delta_x, \delta_y)$ of a neighborhood of the considered site i, noted as $\max(|\delta_x|, |\delta_y|) \leq \delta_{\max}$, where $\delta_{\max}$ is an integer that specifies the farthest neighbor considered in any direction. It is implicitly applied to both δ and δ'. Under that threshold, we consider every combination of δ and δ' that generates a unique, new excitation. The excitations have to be nonredundant (different). Otherwise, they will lead to singular matrices for $\mathbf{H}_{\mathbf{k}}$ and $\mathbf{O}_{\mathbf{k}}$. Note that $|e_{i\sigma n}\rangle$ is in the electron-number sector with one electron added to the ground state, while $|h_{i\sigma n}\rangle$ is in the one-electron-removed sector.

Equation (18) is the simplest choice of basis to reasonably represent the essential part of the low-energy excitation subspace of the Hamiltonian (as demonstrated in the result section). One might be concerned with whether the choice of Eq. (18) exhausts the important excited states that show up in $A(\mathbf{k}, \omega)$. The benchmark in the later section will help us to see the relevance of the basis. However, it is also helpful to examine physical intuition. The basis $|e_{i\sigma n}\rangle$, for instance, contains $c^\dagger_{i,\sigma}|\Omega\rangle$, which is indeed the bare excitation from the ground state in the representation Eq. (3). Of course, it is not the eigenstate of the Hamiltonian in the $N+1$ particle sector. Therefore, the time evolution of the eigenstate represented by the denominator of Eq. (3) must contain other states by considering the correlation effects. In the ground states, the correlation effects are largely taken into account by the correlation factors (Gutzwiller and Jastrow factors, etc.). In the present case, we include $c^\dagger_{i,\sigma}n_{i,\bar{\sigma}}|\Omega\rangle$ as well as $c^\dagger_{i,\sigma}|\Omega\rangle$, which may also be rewritten as the expansion by $n_{i,\bar{\sigma}}c^\dagger_{i,\sigma}|\Omega\rangle$ and $(1-n_{i,\bar{\sigma}})c^\dagger_{i,\sigma}|\Omega\rangle$. The former essentially generates the electrons in the upper Hubbard band, and the latter generates those in the lower Hubbard band. The basis we employ can then represent the correlation factor (Gutzwiller factor) efficiently in the $N+1$-electron sector, not only for the lower-energy weight (lower Hubbard) but also the higher-energy side (upper Hubbard). In addition, $c^\dagger_{i,\sigma}n_{j,\bar{\sigma}}n_{l,\sigma'}|\Omega\rangle$ may essentially represent the Jastrow factor as well. Since $|\Omega\rangle$ contains the spin fluctuations in the ground state, the present excited states contain the same spin fluctuation. Missing in the present excited state is the one-electron-added state generated simultaneously by multiple spin scattering from the ground state. Although it can, in principle, be included in the present formalism as we discuss in the end of this paper, we focus on the choice (18) and leave the one-electron-added state for future study. It is not intuitively clear that we are able to describe the Mott insulating state with upper and lower Hubbard bands. Since the Tomonaga-Luttinger liquid is well described in the ground state [41], it can describe states with a vanishing renormalization factor. Later, we also see that the incoherent continuum can emerge from our excitation basis.

Using this excitation basis, we calculate the average of

$$\langle\psi_{im}|\hat{c}_{i\sigma}\hat{c}^{\dagger}_{j\sigma}|\psi_{jn}\rangle, \qquad \langle\psi_{im}|\hat{c}^{\dagger}_{i\sigma}\hat{c}_{j\sigma}|\psi_{jn}\rangle, \tag{19}$$

$$\langle\psi_{im}|\hat{c}_{i\sigma}\hat{H}\hat{c}^{\dagger}_{j\sigma}|\psi_{jn}\rangle, \qquad \langle\psi_{im}|\hat{c}^{\dagger}_{i\sigma}\hat{H}\hat{c}_{j\sigma}|\psi_{jn}\rangle, \tag{20}$$

in the real space representation for every i, j combination (N^2 terms) using Markov chain Monte Carlo sampling of Eq. (13) for different simple operators. The details of which quantities to sample and how to sample them are presented in Appendix B, along with some details to optimize the computation speed of the calculation of these excitations.

Once we have these terms, we can Fourier transform (thanks to the translational symmetry):

$$O^{e}_{\mathbf{k},mn} = \frac{1}{N_s}\sum_{ij} e^{-i\mathbf{k}(\mathbf{r}_i-\mathbf{r}_j)}\langle\psi_{im}|\hat{c}_{i\sigma}\hat{c}^{\dagger}_{j\sigma}|\psi_{jn}\rangle, \tag{21}$$

$$H^{e}_{\mathbf{k},mn} = \frac{1}{N_s}\sum_{ij} e^{-i\mathbf{k}(\mathbf{r}_i-\mathbf{r}_j)}\langle\psi_{im}|\hat{c}_{i\sigma}\hat{H}\hat{c}^{\dagger}_{j\sigma}|\psi_{jn}\rangle, \tag{22}$$

$$O^{h}_{\mathbf{k},mn} = \frac{1}{N_s}\sum_{ij} e^{-i\mathbf{k}(\mathbf{r}_i-\mathbf{r}_j)}\langle\psi_{im}|\hat{c}^{\dagger}_{i\sigma}\hat{c}_{j\sigma}|\psi_{jn}\rangle, \tag{23}$$

$$H^{h}_{\mathbf{k},mn} = \frac{1}{N_s}\sum_{ij} e^{-i\mathbf{k}(\mathbf{r}_i-\mathbf{r}_j)}\langle\psi_{im}|\hat{c}^{\dagger}_{i\sigma}\hat{H}\hat{c}_{j\sigma}|\psi_{jn}\rangle. \tag{24}$$

These Fourier transforms produces a number of matrices with as many as twice the number of momentum points. With these matrices, we solve the generalized eigenvalue problem [Eq. (8)] for both holes and electrons.

Together with Eqs. (1), (9), and (10), we estimate the Green's function from the VMC. We call the technique presented in this section dynamical VMC (dVMC).

E. Summary of the technique

Since this new technique requires multiples steps, we summarize our algorithm for convenience by listing the sequential procedure here:

(1) The ground state $|\Omega\rangle$ and its energy Ω are calculated using the definition (14) and minimizing Eq. (11) through the variational Monte Carlo sampling of Eq. (13).

(2) The terms (19) and (20) are calculated by using variational Monte Carlo sampling (13) distinct from the ground-state sampling because $|\psi_{\mathrm{in}}\rangle$ defined in Eq. (18) constitutes a Hilbert space extended from the ground state $|\psi\rangle = |\Omega\rangle$.

(3) The Fourier transform [Eqs. (21)–(24)] is used to obtain the matrices in Eqs. (6) and (7).

(4) We solve the eigenvalue problem Eq. (8) for both hole and electron excitations and obtain $|E^{h}_{\mathbf{k}l}\rangle$ and $|E^{e}_{\mathbf{k}l}\rangle$.

(5) We calculate the Green's function in Eqs. (9) and (10) by substituting $|\Omega\rangle$ obtained in step 1 and $|E^{h}_{\mathbf{k}l}\rangle$ and $|E^{e}_{\mathbf{k}l}\rangle$ obtained in step 4 above, or through the application of Eq. (A4), as implemented now in the dVMC source code provided in the Supplemental Material [34].

Both variational Monte Carlo steps (1 and 2) take the most computational time. The computational cost of the ground-state determination (step 1) scales as $N_{\mathbf{s}} \times O(N_p^3)$, where N_p is the number of variational parameters f_{ij}, g_i, and v_{ij} defined in Eq. (14) [35] and $N_{\mathbf{s}}$ is the number of Monte Carlo samples. Some constraints can and must be used at times to reduce the degrees of freedom (N_p) of the variational ground states and thus reduce the calculation time. The computational cost of sampling the terms in Eqs. (19) and (20) (step 2) scales as $N_{\mathbf{s}} \times N_{\mathrm{exc}} \times O(N_p^3) \times O(N^2(1+2N_t))$, where N, N_t, and N_{exc} are the number of lattice points, hoppings for each site, and excitations, respectively. The excitation scheme [Eq. (18)] offers many excitations with a relatively low computational cost in step 2. In Appendix B, we discuss more details of the optimization of the calculation.

III. RESULTS

A. Model

To examine the accuracy of the present dynamical VMC method, we show the benchmark test of the standard Hubbard model with the Hamiltonian

$$\hat{H} = -t\sum_{\langle i,j\rangle,\sigma}\hat{c}^{\dagger}_{i\sigma}\hat{c}_{j\sigma} + U\sum_{i}\hat{n}_{i\uparrow}\hat{n}_{i\downarrow} \tag{25}$$

on the 1D chain and 2D square lattice. The first term proportional to the transfer t is the kinetic energy, and the sum is restricted to the nearest-neighbor pair. The second term represents the on-site Coulomb repulsion proportional to U. We impose periodic boundary conditions throughout this paper. In the presentation, the same color scale is used to make the comparison between different methods and sizes easier, except for Fig. 7. Unless otherwise specified, we use parameters $U = 8$ and the nearest-neighbor transfer $t = 1$ as the energy unit. We use the broadening factor $\eta = 0.2$. The chemical potential (Fermi level) is determined so as to meet the occupied part of the integrated spectral weight with the number of electrons ($N_e =$ integer) given in our canonical ensemble simulation of VMC. Results obtained by the present method on lattices of $N = 16$ sites are first compared to ED results in order to benchmark the accuracy of the methods in one and two dimensions.

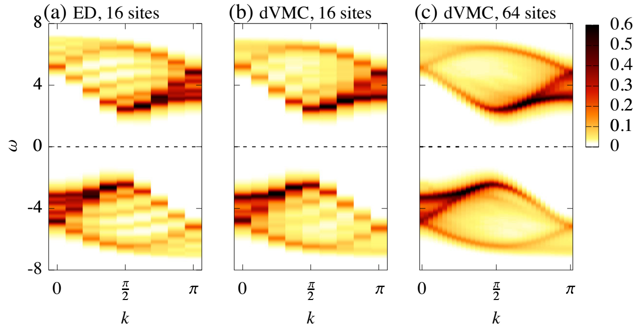

FIG. 2. Comparison of spectral weight for the 1D Hubbard model at half-filling ($L = 16$ and $N_e = 16$) calculated by the ED (a) and by the present method dVMC (b). For the 16-site dVMC calculation, we considered combinations of every possible neighbor for the choice of δ and δ' in Eq. (18). Since the size is small, $N_{\mathrm{exc}} = 377$ excitations are considered, in total, by omitting redundant excitations. In panel (c), we show the result for dVMC with 64 sites. We consider up to $\delta_{\max} = 8$, resulting in a total of $N_{\mathrm{exc}} = 426$ excitations.

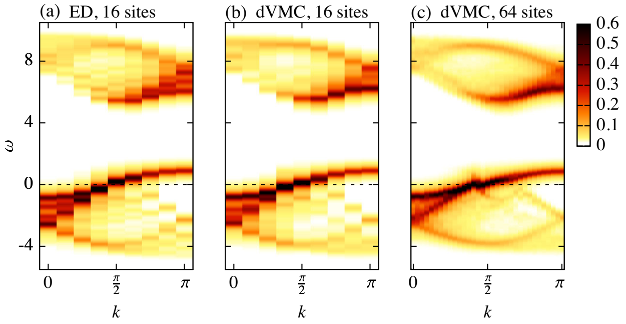

FIG. 3. Comparison of spectral weight for the doped 1D Hubbard model at $U/t = 8$ ($L = 16$ and $N_e = 14$) (b) with the ED result (a). (c) Results of lightly doped 64-site chain ($N = 64$ and $N_e = 56$). Here, $\omega = 0$ is the Fermi level. The choices of δ and δ' for panels (b) and (c) are the same as in Fig. 2.

The ED results were obtained using the open-source software HΦ [42].

Symmetries are imposed via some constraints in the variational parameters f_{ij}, g_i, and v_{ij} of the trial wave function. We do not impose any symmetry for the one-dimensional case, but we impose a 2×2 sublattice structure to allow for a description of the antiferromagnetic states for the two-dimensional case. Imposing this sublattice structure will prevent the emergence of any stripe or charge order, for example. Note, however, that it is possible to study the charge order using VMC [32] and dVMC, but this is beyond the scope of the present article. The variational wave function [Eq. (14)] can represent the Mott insulator due to the doublon-holon binding correlations in the Jastrow factor [43].

B. One-dimensional lattice

In this section, we show the various results for the one-dimensional Hubbard model. We first test both the Mott insulator ($N = N_e$) and the doped Mott insulator in the one-dimensional Hubbard model by comparing with the exact diagonalization results for the 16-site chain. The results at half-filling are shown in Fig. 2(b), in comparison with exact diagonalization results in Fig. 2(a). We see that the present dVMC results show nearly perfect and quantitative agreement with the Mott insulating nature between the results of the present method and the ED in terms of the dispersion of the lower (occupied) Hubbard band below E_F and the upper (unoccupied) Hubbard band above E_F, in terms of their broadness, relative weights, and the Mott gap sizes. A direct superposition of the $A(k,\omega)$ curves for selected k points is shown in Appendix C in order to provide a more quantitative comparison.

The results for the 64-site chain are shown in Fig. 2(c), which gives much higher momentum resolution. Both in the 16-site and 64-site results, the lower (upper) Hubbard dispersion below (above) E_F splits into two dispersions around the Γ ($k = 0$) and $k = \pi$ points. The upper, flat dispersion branch in the lower Hubbard dispersion is identified as the spinon branch, and the lower, steeper dispersion branch is identified as coming from the holon excitation in the analysis of the ARPES data for $\mathrm{SrCuO_2}$ [44,45]. The present dVMC calculation correctly captures the spin-charge separation in the 1D Hubbard model. We also note that the spin-charge separation at the heart of the Tomonaga-Luttinger liquid was correctly captured in Ref. [28].

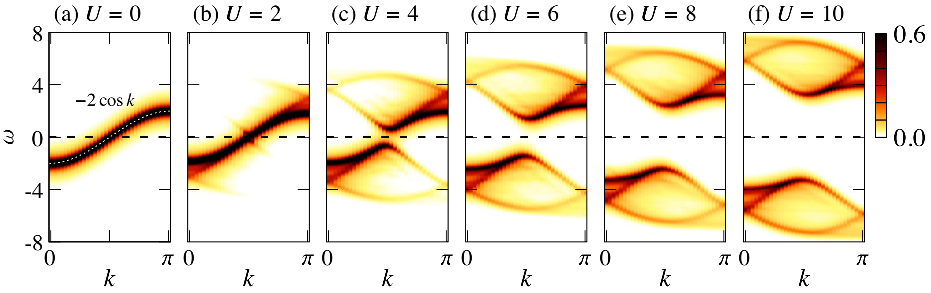

FIG. 4. Mott transition calculated from dVMC with 64 sites on the 1D Hubbard model at half-filling. Different panels show different interaction strengths U.

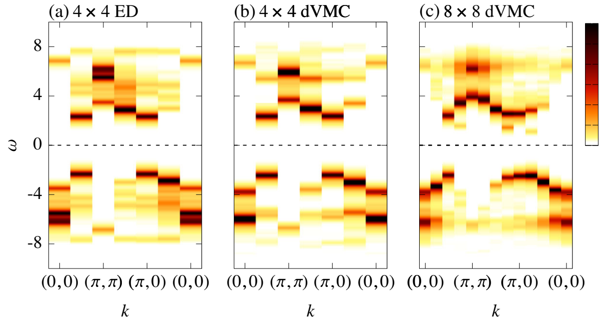

FIG. 5. Comparison of spectral weight $A(k,\omega)$ in the momentum-energy plane for the square-lattice Hubbard model at half-filling ($N = 4 \times 4$ and $N_e = 16$) calculated by ED (a) and by dVMC (b). For the 16-site dVMC calculation, we consider combinations of every possible neighbor for the choice of δ and δ' in Eq. (18). In total, $N_{\mathrm{exc}} = 377$ excitations are taken into account after omitting redundant excitations. The result of the same quantity for the 8×8 lattice is shown in panel (c), which shows an essential agreement with the result of cluster perturbation theory [47,48]. In panels (a)–(c), $A(k,\omega)$ is plotted along the symmetric line of the momentum in the Brillouin zone.

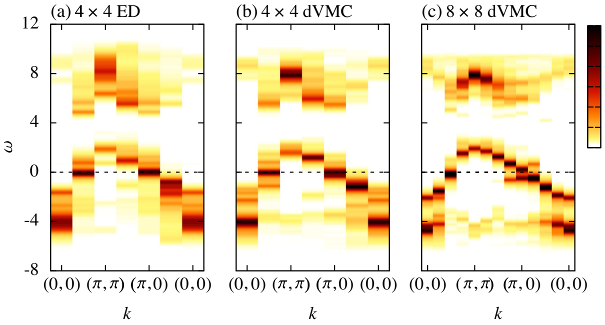

FIG. 6. Spectral weight for the doped square-lattice Hubbard model ($N = 4 \times 4$ and $N_e = 14$) in panel (b) compared with the ED result in panel (a). The result of the 8×8 lattice with $N_e = 56$ at 12.5% hole doping is shown in panel (c). The momentum dependence is shown along the symmetric line in the same way as in Fig. 5. Here, $\omega = 0$ is the Fermi level.

The doped case is shown in Fig. 3. The comparison between the dVMC result in panel (b) and the ED result in panel (a) for the doping concentration $\delta = 0.125$ again shows nearly perfect agreement. The same doping for the 64-site systems in Fig. 3(c) shows good agreement with the result obtained by Kohno using the dynamical density-matrix renormalization group (DDMRG) for a 60-site system with the open boundary condition [46,47]. We still see both the holon and spinon bands. We also note the presence of the hole-pocket behavior appearing at the Fermi level [46]. We show the dependence on the number of excitations taken into account in Appendix D.

Finally, we show in Fig. 4 the Mott transition by varying the interaction strength U for the half-filled case. At $U = 0$, we find exactly $-2\cos k$, which is to be expected for this system without an interaction. Note that $U = 10$ corresponds to the result published with DDMRG [47]. The gap opens gradually as the interaction U increases from 0 to 10. It is to be noted that the Mott gap at $U = 2$ is not visible since the Lorentzian broadening factor $\eta = 0.2$ smears the fine structure expected around the Fermi level. This case explicitly shows that the technique does not have a specific interaction regime and can perform well in both U limits. For the rest of the paper, we employ $U = 8$.

C. Two-dimensional square lattice

In this section, we examine the square lattice, both for the Mott insulator ($N = N_e$) (see Fig. 5) and the doped Mott insulator (Fig. 6). Comparison of the dVMC results in Figs. 5(b) and 6(b) with the exact diagonalization results in Figs. 5(a) and 6(a), respectively, proves good accuracy of the dVMC method even for the 2D lattice. The comparison of the 8×8 lattice results in Fig. 5(c) at half-filling and Fig. 6(c) at 12.5% hole doping with the result of the cluster perturbation theory [47,48] and quantum Monte Carlo [49] shows a fair overall agreement. Note that the results of the cluster perturbation [47,48] has lower momentum resolution and should not be taken as a sufficiently accurate reference. Also, the quantum Monte Carlo results [49] at half-filling are not at $U = 8$ but have the same qualitative features. The incoherent continuum is less clear in QMC results than our dVMC results, but this is probably an effect of the analytic continuation of QMC. Therefore, a small discrepancy does not necessarily mean that the present results are insufficient.

In both Figs. 5(c) and 6(c), we have employed a 2×2 sublattice to constrain the ground state to exclude stripe orders as well as x-y anisotropies [32]. Figure 6(c) shows results for a low-energy state, which has a superconducting order with $d_{x^2-y^2}$ symmetry. Note that the true ground state may have the stripe order without any superconducting order [31–33]. However, the superconducting state is very close to the ground state and is obtained at least as a well-optimized metastable state. Therefore, we could expect to be able to see the intrinsic property of the superconducting phase when it is stabilized in a realistic Hamiltonian [50]. The superconducting correlation function for this state confirms the superconducting long-range order (see Appendix E).

To have a better view of the superconducting physics, we obtain results on a bigger cluster. In Fig. 7, we examine a 12×12 cluster with the same parameters as in Fig. 6(c). We see similarities between Figs. 7(a) and 6(c) but with much more details. To see the detailed structure of the gap, we first plot, in Figs. 7(b)–7(d), the spectral weight in the Brillouin zone for energies at and near the Fermi level, namely, $\omega = -0.3$, 0.0, and 0.3, to estimate the position of the gap opening (in other words, the locus of the minimum gap, which should form the Fermi surface when the gap closes). In principle, the locus of the gap opening can be

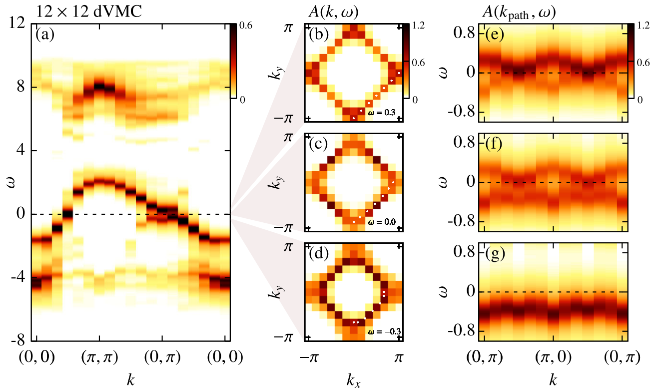

FIG. 7. Spectral function $A(k,\omega)$ for a 12×12 cluster. (a) Same view as in Fig. 6(c). (b)–(d) Spectral function for a constant energy at and around the Fermi level ($\omega = 0.0$) plotted in the Brillouin zone. Energies are, respectively, $\omega = 0.3$, 0.0, and -0.3. (e)–(g) Spectral function in the momentum-energy plane, with the momentum following the symmetric line along $(0,\pi) - (\pi,0) - (0,\pi)$. The labels of the $\mathbf{k}$ axis on the abscissa in these panels show only the points on the trajectory of white dots closest to the symmetric points because the white-dot trajectory is not precisely along the symmetric line. We follow the maximum intensity lines in the Brillouin zone of the corresponding panel on the left. The choice of k points in the path in panel (e) is shown with the white dots in the corresponding panel on the left [panel (b)]. The same is true for panels (c) and (f) and for panels (d) and (g), but in these cases, we use linear interpolations to more precisely identify the paths away from the discrete k points. The superconducting d-wave gap structure is clearly seen in panel (f). Note that in this figure, panel (a) has the same color scale as the rest of the paper, but panels (b)–(g) have another color scale (shown in the top right), in order to see more clearly the details in the superconducting gap and around the Fermi level.

inferred from the maximum intensity of $A(k,\omega=0)$. The gap anisotropy can be seen along this trajectory. However, because of the limited discrete points in the Brillouin zone allowed for finite-size studies, a better estimate of the gap opening position is obtained by an interpolation of $A(k,\omega)$ between neighboring momentum points using the data at small but nonzero ω as well. In fact, the rough estimate of the largest gap indicates that it appears at the antinode with amplitude $\Delta \sim 0.3t$. At $\omega/t = -0.3$, 0.0, and 0.3, we also show the obtained trajectory of the maximum $A(k,\omega)$ intensity with white dots and the corresponding interpolated spectral weight for these dots on the right panels [(e)–(g)]. It is important to interpolate between different ω because the Fermi level determined from the consistency between the electron number in the occupied part of $A(k,\omega)$ and the given nominal number itself has uncertainty arising from the discrete k points and the broadening factor. In addition, because of the gap, it contains another uncertainty in precisely identifying the gap-opening position in Fig. 7(c). Nevertheless, in Fig. 7(f), we can see clearly that the gap anisotropy is essentially expressed by the d-wave superconducting gap [$\Delta(\mathbf{k}) = (\Delta/2)(\cos k_x - \cos k_y)$], which has a maximum at the antinodes [$\mathbf{k} = (0,\pm\pi), (\pm\pi,0)$] and closes at the nodes ($k_x = k_y$), though the precise functional form of the gap is beyond the scope of the present paper.

Note that the number of excitations, for the case in Figs. 6(c) and 7, have been limited to 118 excitations, by keeping only the ranges $0 \le \delta_x^{(l)} \le 2$ and $0 \le \delta_y^{(l)} \le 2$ to suppress the statistical error within our allowed computational cost.

The ratio $V_d = \Delta/F$, with $F = \sqrt{P_d(r\to\infty)}$ being the superconducting order parameter $\langle\Delta_d\rangle$, is the measure of the effective attractive interaction to form the Cooper pair. From Fig. 11 in Appendix E, $\langle\Delta_d\rangle$ is estimated to be 0.055. Then, the attractive interaction is roughly estimated as $V_d \sim 1.7t$, which is extremely large, implying that the superconductivity in the Hubbard model is unrealistically strong if we take it as a model of the cuprate superconductors with $t \sim 0.5$ eV as employed in the literature. In fact, the gap size itself is estimated to be about $0.3t$ at $U = 8$, which is a realistic value of the cuprates [50]. In this range, the gap amplitude increases with U, in contrast to the expectation from the exchange interaction $J = 4t^2/U$. The value $0.3t$ is interpreted as about 150 meV for the cuprates, which is three times larger than the gap amplitude of about 50 meV measured in the cuprates [1,2]. However, as we mentioned above, the true ground state for this doping should be the charge-inhomogeneous stripe state because of such a strong attraction.

A possible origin of the effective attraction is the energy gain by the recovery of the electron coherence (fading out of Mottness), which grows nonlinearly with the doping. This nonlinear reduction of the kinetic energy generates a strong upward convex curve of the electronic energy as a function of the carrier density. This negative curvature signals the effective attractive interaction of charge carriers because the quadratic term obviously represents the effective electron-electron interaction [51]. The attractive interaction estimated from the negative curvature again has the same order, consistent with the present value of about t [52].

By using the present method, we have shown that the d-wave gap of the Hubbard model has an energy scale of t (more precisely, about $0.3t$), which is much larger than the value of the model of the cuprate superconductors. We note that a more realistic understanding of the scale of the attraction of the cuprates and other available superconductors has to be reached by using the *ab initio* effective Hamiltonian that has realistic nonzero off-site Coulomb repulsions [50].

D. Computational cost

In this section, we discuss the typical computational cost for a few of the systems calculated. Let us stress that these values are highly dependent on the number of variational parameters N_p, sites N, samples $N_\mathbf{s}$, and hopping terms N_t, as discussed in Sec. II E. Computations of the smallest systems (16 sites) can be performed on a desktop computer in under a few hours. But for the sake of comparison, we present the time required to perform the calculations on the same supercomputer at the Institute for Solid State Physics. All of the calculations have been performed using multiple nodes (via MPI) of each 24 CPU (via OpenMP).

For the one-dimensional case with $N = 16$ sites ($N_t = 2$ and $N_p = 392$), using $N_\mathbf{s} = 7.2 \times 10^5$ for the ground-state calculation (step 1 of Sec. II E) required 8 minutes. Using $N_\mathbf{s} = 1.8 \times 10^5$ and $N_\mathrm{exc} = 377$ for the sampling of the terms (19) and (20) (step 2 of Sec. II E) required 3 minutes. In total, this calculation required 11 minutes on 240 CPU.

For the one-dimensional case with $N = 64$ sites ($N_t = 2$ and $N_p = 6176$), using $N_\mathbf{s} = 5.76 \times 10^5$ for step 1 required 4.5 hours, and using $N_\mathbf{s} = 2.6 \times 10^6$ and $N_\mathrm{exc} = 426$ for step 2 required 5.5 hours, for a total of 10 hours on 3456 CPU.

For the two-dimensional case with $N = 144$ sites ($N_t = 4$ and $N_p = 872$), using $N_\mathbf{s} = 5.76 \times 10^5$ for step 1 required 1.5 hours, and using $N_\mathbf{s} = 8.64 \times 10^5$ and $N_\mathrm{exc} = 118$ for step 2 required 11.5 hours, for a total of 13 hours on 3456 CPU.

These numbers are the ones used for the calculation of Figs. 2(b), 2(c), and 7, respectively. The calculation time increases with system size. For the 12×12 case, the time is comparable to the one-dimensional chain of 64 sites due to the use of many symmetries and the reduction of the excitation number considered.

IV. SUMMARY AND OUTLOOK

In this paper, we examined a newly proposed dVMC method to calculate the single-particle spectral function and the Green's function for strongly correlated electron systems. Although the proposed variational form of the excited states is simple and contains only one bare electron or hole added to the ground state—dressed by composite operators diagonal in the particle-number representation—the obtained spectral function rather accurately reproduces the exact structure in the benchmark.

An application to the hole-doped square-lattice Hubbard model revealed that a *d*-wave superconducting state is induced by an effective carrier attraction, which is unexpectedly large ($\sim 0.3t$), resulting in a much larger superconducting gap than that observed in the corresponding cuprates, if we study the charge-uniform lowest-energy state as the ground state. It implies that the real cuprate superconductors have to be understood by taking account of more realistic factors such as the intersite Coulomb repulsion, which suppresses both the charge inhomogeneity and the superconducting order overestimated in the Hubbard model in comparison to the real, existing superconductors [50].

Though it reached unprecedented and fruitful results, the obtained spectral function is not perfect, with some discrepancy from the exact results. We note that spectral functions are very sensitive to the ground state $|\Omega\rangle$ used in the calculation and strongly compete with other metastable states. The sensitivity requires a high accuracy of the ground-state wave function before calculating the dVMC Green's function. In addition, the form of the excited states has to be flexible enough, particularly, to represent low-energy excitations. Qualitatively different types of excitations ignored in the present work but presumably important are the dressing by the spin-flip excitation such as $\hat{c}^\dagger_{i+\delta,\sigma}\hat{c}_{i+\delta,\bar{\sigma}}\hat{c}^\dagger_{i,\bar{\sigma}}|\Omega\rangle$ and that by kinetic operators such as $\hat{c}^\dagger_{i+\delta,\sigma}\hat{c}_{j+\delta,\sigma}c^\dagger_{i,\sigma}|\Omega\rangle$, which are off diagonal in the particle-number representation. The inclusion of these excitations is an intriguing future issue, which might enhance the accuracy. Of course, increasing the number of charge operators as $\hat{n}_{i,\bar{\sigma}}\hat{n}_{i+\delta'_n,\sigma}\hat{n}_{i+\delta''_n,\bar{\sigma}}|\Omega\rangle$, $\hat{n}_{i,\bar{\sigma}}\hat{n}_{i+\delta'_n,\sigma}\hat{n}_{i+\delta''_n,\sigma}|\Omega\rangle$ may also improve the accuracy.

In fact, such an improvement in the present dVMC method is expected to contribute to a better understanding of the low-energy subtle structures such as the pseudogap and the effect of severe competition among superconducting, charge, and spin correlations of the doped Mott insulator.

ACKNOWLEDGMENTS

We acknowledge Youhei Yamaji, Kota Ido, Takahiro Ohgoe, and Shiro Sakai for fruitful discussions. This work was supported by Fonds de Recherche du Québec–Nature et Technologies (FRQNT) and by a Grant-in-Aid for Scientific Research (No. 16H06345) from the Ministry of Education, Culture, Sports, Science and Technology, Japan. The authors are grateful to the MEXT HPCI Strategic Programs, and the Creation of New Functional Devices and High-Performance Materials to Support Next Generation Industries (CDMSI) for their financial support. We also acknowledge the support provided by MEXT through "Basic Science for Emergence and Functionality in Quantum Matter—Innovative Strongly-Correlated Electron Science by Integration of *Fugaku* and Frontier Experiments," a program for promoting research on the supercomputer Fukaku, supported by RIKEN Center for Computational Science (R-CCS) through HPCI System Research Project (Project ID: hp180170, hp190145, and hp200132). Part of the computation was done at the Supercomputer Center, Institute for Solid State Physics, University of Tokyo.

APPENDIX A: ALTERNATIVE PROOF

In this appendix, we show the Green's function calculation as is implemented in the dVMC code, which is available in the Supplemental Material [34]. It is an alternative form of Eqs. (9) and (10).

The Green's function in a nonorthogonal basis is also expressed as [53]

$$\mathbf{G}_h(\mathbf{k},\omega) = \mathbf{O}_{h\mathbf{k}}((\omega + i\eta - \Omega)\mathbf{O}_{h\mathbf{k}} + \mathbf{H}_{h\mathbf{k}})^{-1}\mathbf{O}_{h\mathbf{k}}, \tag{A1}$$

$$\mathbf{G}_e(\mathbf{k},\omega) = \mathbf{O}_{e\mathbf{k}}((\omega + i\eta + \Omega)\mathbf{O}_{e\mathbf{k}} - \mathbf{H}_{e\mathbf{k}})^{-1}\mathbf{O}_{e\mathbf{k}}, \tag{A2}$$

which are related to the abstract Green's operators $\hat{G}_h(\mathbf{k},\omega)$ and $\hat{G}_e(\mathbf{k},\omega)$ defined as

$$\mathbf{G}_h(\mathbf{k},\omega)|_{mn} = \langle h_{\mathbf{k}m}|((\omega + i\eta - \Omega)\hat{I} + \hat{H})^{-1}|h_{\mathbf{k}n}\rangle,$$
$$\mathbf{G}_e(\mathbf{k},\omega)|_{mn} = \langle e_{\mathbf{k}m}|((\omega + i\eta + \Omega)\hat{I} - \hat{H})^{-1}|e_{\mathbf{k}n}\rangle.$$

From these definitions, we see that if we choose the first excitations such that $\hat{B}_0 = \hat{I}$, we obtain the Green's function (1), with

$$G_{\mathbf{k}\sigma}(\omega) = (\mathbf{G}_e(\mathbf{k},\omega) + \mathbf{G}_h(\mathbf{k},\omega))_{m=n=0}. \tag{A3}$$

To speed up calculations, we can rearrange and diagonalize the terms $\mathbf{H}_{h\mathbf{k}}\mathbf{O}_{h\mathbf{k}}^{-1}$ and $\mathbf{H}_{e\mathbf{k}}\mathbf{O}_{e\mathbf{k}}^{-1}$ in Eqs. (A1) and (A2):

$$G_{\mathbf{k}\sigma}(\omega) = \sum_l \frac{(\mathbf{U}_{h\mathbf{k}})_{0l}(\mathbf{U}_{h\mathbf{k}}^{-1}\mathbf{O}_{h\mathbf{k}})_{l0}}{\omega + i\eta - \Omega + E_{h\mathbf{k},l}} + \frac{(\mathbf{U}_{e\mathbf{k}})_{0l}(\mathbf{U}_{e\mathbf{k}}^{-1}\mathbf{O}_{e\mathbf{k}})_{l0}}{\omega + i\eta + \Omega - E_{e\mathbf{k},l}}, \tag{A4}$$

where the energies $E_{\mathbf{k},l}$ are the eigenvalues and $\mathbf{U}_\mathbf{k}$ are the eigenvector matrices. Note that even if both matrices $\mathbf{H}_\mathbf{k}$ and $\mathbf{O}_\mathbf{k}^{-1}$ are Hermitian, their product is not. Hence, $\mathbf{U}_\mathbf{k}$ is not unitary. This form is equivalent to Eqs. (9) and (10).

APPENDIX B: SAMPLED QUANTITIES

The bottleneck of the calculation of $O_{\mathbf{k},mn}$ and $H_{\mathbf{k},mn}$ for both the hole and the electron is the Monte Carlo sampling with a charge configuration $|x_\mathbf{s}\rangle$ of the quantities:

$$g_{ij,\sigma}(x_\mathbf{s}) = \langle\Omega|\hat{c}_{i\sigma}^\dagger\hat{c}_{j\sigma}|x_\mathbf{s}\rangle, \tag{B1}$$

$$g_{ijkl,\sigma\sigma'}(x_\mathbf{s}) = \langle\Omega|\hat{c}_{i\sigma}^\dagger\hat{c}_{j\sigma}\hat{c}_{k\sigma}^\dagger\hat{c}_{l\sigma}|x_\mathbf{s}\rangle, \tag{B2}$$

for $0 \le i, j < N$ and k, l are the indices of every hopping on the cluster. This calculation then requires $2N^2(1 + 2N_t)$ Pfaffian evaluations in total (where N_t is the number of hoppings in the cluster) for the simple Hubbard model. When we have all the values of Eqs. (B1) and (B2) in hand, from these values alone, we can deduce

$$\langle\psi_{im}|\hat{c}_{i\sigma}\hat{c}_{j\sigma}^\dagger|\psi_{jn}\rangle, \qquad \langle\psi_{im}|\hat{c}_{i\sigma}^\dagger\hat{c}_{j\sigma}|\psi_{jn}\rangle, \tag{B3}$$

$$\langle\psi_{im}|\hat{c}_{i\sigma}\hat{H}\hat{c}_{j\sigma}^\dagger|\psi_{jn}\rangle, \qquad \langle\psi_{im}|\hat{c}_{i\sigma}^\dagger\hat{H}\hat{c}_{j\sigma}|\psi_{jn}\rangle \tag{B4}$$

straightforwardly by using (anti)commutation relations of fermion operators for the simple Hubbard model. These quantities are the same as Eqs. (19) and (20).

First, since the inserted state $|x_\mathbf{s}\rangle$ in the VMC sampling method (11) is a real space configuration, the evaluation of any $\hat{n}_{i\sigma}$ is fast since $\hat{n}_{i\sigma}|x_\mathbf{s}\rangle = |x_\mathbf{s}\rangle n_{i\sigma}(x_\mathbf{s})$, where $n_{i\sigma}(x_\mathbf{s})$ is a scalar: 1 if the site i of spin σ is occupied, and 0 otherwise. The set of charge diagonal operators on the left-hand side can be moved to the right analytically until they reach $|x_\mathbf{s}\rangle$. For this purpose, we use the relation

$$\hat{n}_a\left(\prod_i\hat{c}_i^\dagger\prod_j\hat{c}_j\right) = \left(\prod_i\hat{c}_i^\dagger\prod_j\hat{c}_j\right)\left(\hat{n}_a + \sum_i\delta_{ia} - \sum_j\delta_{ja}\right) \tag{B5}$$

to commute any charge operator from left to right (which holds for any order of $\hat{c}_i^\dagger$ and $\hat{c}_j$). The terms in Eq. (B3) and the interaction part ($\hat{H}_U$) of Eq. (B4) can thus all be computed from the values

$$\langle\Omega|\hat{c}_{i\sigma}\hat{c}_{j\sigma}^\dagger|x_\mathbf{s}\rangle = \delta_{ij} - g_{ji,\sigma}(x_\mathbf{s}), \tag{B6}$$

$$\langle\Omega|\hat{c}_{i\sigma}^\dagger\hat{c}_{j\sigma}|x_\mathbf{s}\rangle = g_{ij,\sigma}(x_\mathbf{s}), \tag{B7}$$

and the hopping part ($\hat{H}_t$) of Eq. (B4) can be computed from

$$\langle\Omega|\hat{c}_{i\sigma}\hat{c}_{k\sigma'}^\dagger\hat{c}_{l\sigma'}\hat{c}_{j\sigma}^\dagger|x_\mathbf{s}\rangle = -g_{jikl,\sigma\sigma'}(x_\mathbf{s}) + \delta_{ij}g_{kl,\sigma'}(x_\mathbf{s}) + \delta_{jl}\delta_{\sigma\sigma'}(\delta_{ik} - g_{ki,\sigma}(x_\mathbf{s})), \tag{B8}$$

$$\langle\Omega|\hat{c}_{i\sigma}^\dagger\hat{c}_{k\sigma'}^\dagger\hat{c}_{l\sigma'}\hat{c}_{j\sigma}|x_\mathbf{s}\rangle = g_{ijkl,\sigma\sigma'}(x_\mathbf{s}) - \delta_{jk}\delta_{\sigma\sigma'}g_{il,\sigma}(x_\mathbf{s}). \tag{B9}$$

This case reduces the number of Pfaffian calculations. In principle, it generates terms for every $0 \le i, j < N$, but it is convenient to impose the translational invariance at every Monte Carlo sample, if it is satisfied, to reduce the memory cost and Monte Carlo noise. In doing so, only the terms $i = 0$ and $0 \le j - i < N$ need to be computed. Finally, it is important to impose hermiticity at every sampling, too, so that

$$\langle\psi_{im}|\hat{c}_{i\sigma}\hat{c}_{j\sigma}^\dagger|\psi_{jn}\rangle = (\langle\psi_{im}|\hat{c}_{i\sigma}\hat{c}_{j\sigma}^\dagger|\psi_{jn}\rangle + \langle\psi_{jn}|\hat{c}_{j\sigma}\hat{c}_{i\sigma}^\dagger|\psi_{im}\rangle^\star)/2, \tag{B10}$$

$$\langle\psi_{im}|\hat{c}_{i\sigma}\hat{H}\hat{c}_{j\sigma}^\dagger|\psi_{jn}\rangle = (\langle\psi_{im}|\hat{c}_{i\sigma}\hat{H}\hat{c}_{j\sigma}^\dagger|\psi_{jn}\rangle + \langle\psi_{jn}|\hat{c}_{j\sigma}\hat{H}\hat{c}_{i\sigma}^\dagger|\psi_{im}\rangle^\star)/2, \tag{B11}$$

and so on. These two optimizations greatly reduce noise in the resulting data.

APPENDIX C: COMPARISON BETWEEN ED AND dVMC

In Fig. 10, we show selected k points for $A(k,\omega)$ of the previous results of Figs. 2, 3, 5, and 6 for the same graphs in order to facilitate the comparison between ED and dVMC. As stated in the main text, the agreement is very close.

APPENDIX D: DEPENDENCE OF ACCURACY ON THE LEVEL AND NUMBER OF INCLUDED EXCITATIONS

In this appendix, we show the effect of increasing the range $\delta_{\max}$ in Eq. (18).

In Figs. 8 and 9, we show the dependence on the number of excitations for the result presented in Figs. 2(c) and 3(c),

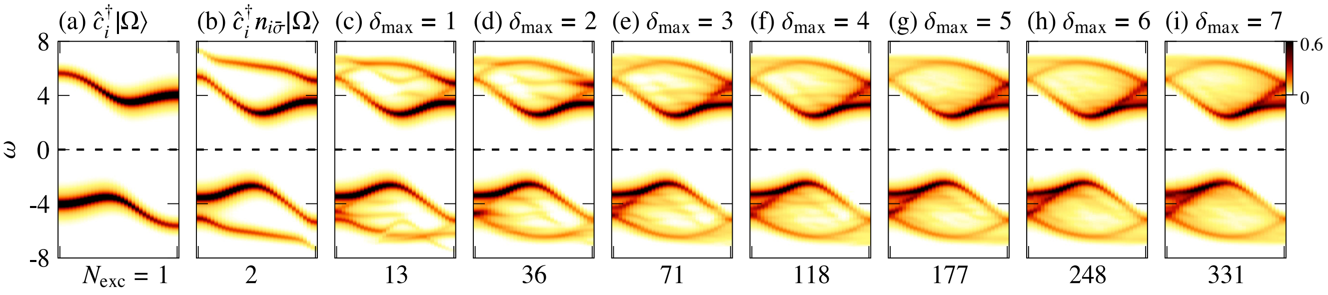

FIG. 8. Comparison of spectral weight for the 64-site 1D Hubbard model in the Mott insulating state, as shown in Fig. 2(c), but considering only a subset of excitations. Indeed, in Fig. 2(c), we consider up to a threshold $\delta_{\max} = 8$. Here, we show the result for $\delta_{\max} = 7$ in panel (i), $\delta_{\max} = 6$ in panel (h), and so on. Panel (b) plots the case where the first two (local) excitations of Eq. (18) are taken into account, and panel (a) is the case taking into account only the first one, i.e., the trivial excitation. Note that the labels in the **k** axis are the same as in Fig. 2(c), so they have been omitted here.

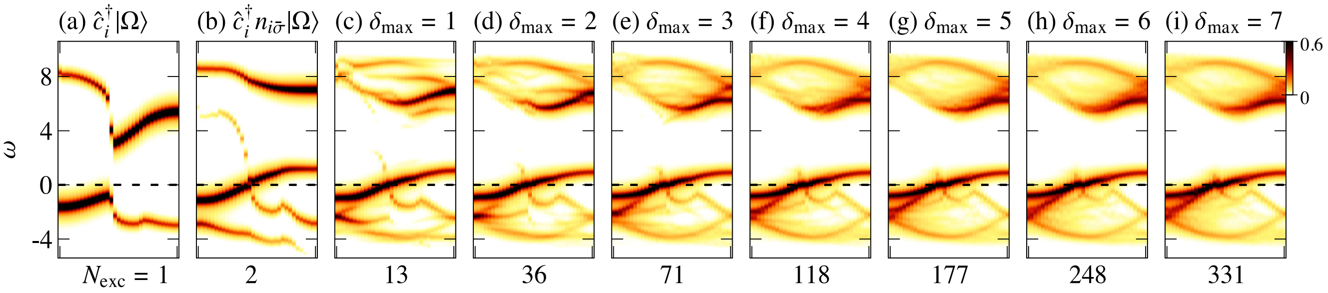

FIG. 9. Comparison of spectral weight for the 64-site 1D Hubbard model at 12.5% hole doping, as shown in Fig. 3(c), but considering only a subset of excitations. Details are the same as in Fig. 8.

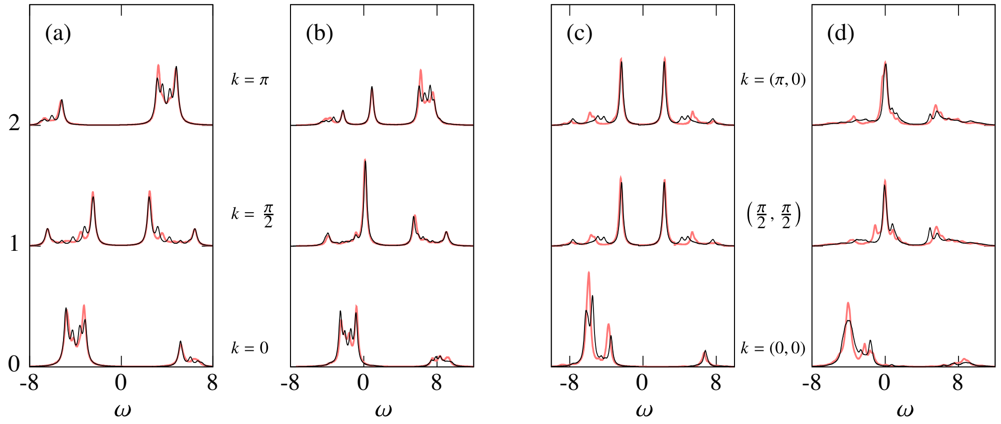

FIG. 10. Comparison between $A(k,\omega)$ obtained from ED (thin black line) and dVMC (thick red line) corresponding to (a) the first two panels of Fig. 2(b) Fig. 3(c) Fig. 5, and (d) Fig. 6. We only show a selection of the most relevant k points, namely, $k = 0$, $\pi/2$, π for panels (a) and (b) and $k = (0,0)$, $(\pi/2, \pi/2)$, $(\pi, 0)$ for panels (c) and (d).

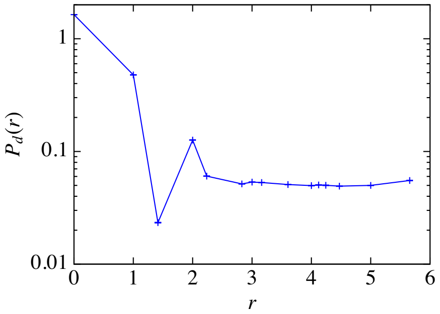

FIG. 11. Superconducting correlation function $P_d(r)$ as a function of pair-pair distance r. The cross data points also contain (very small) error bars.

respectively. We see that the first few neighbors are crucial to get better results. Between $\delta_{\max} = 6$ and $\delta_{\max} = 7$, the result does not change much even if we add 83 new excitations, suggesting the overall convergence to the exact results, aside from the detailed thin structures near the Fermi level in Fig. 9.

APPENDIX E: SUPERCONDUCTING GROUND STATE

The solution presented in Fig. 6(c) has a superconducting order, which can be seen from the gap in the spectral weights plotted in both Figs. 6(c) and 7. This case can be seen more directly by measuring the d-wave superconducting correlation function

$$P_d(\mathbf{r}) = \frac{1}{2N_s}\sum_i \langle \Delta_d^\dagger(\mathbf{r}_i)\Delta_d(\mathbf{r}_i+\mathbf{r}) + \Delta_d(\mathbf{r}_i)\Delta_d^\dagger(\mathbf{r}_i+\mathbf{r})\rangle, \tag{E1}$$

with

$$\Delta_d(\mathbf{r}_i) = \frac{1}{\sqrt{2}}\sum_r g(\mathbf{r})(c_{r_i\uparrow}c_{r_i+r\downarrow} - c_{r_i\downarrow}c_{r_i+r\uparrow}), \tag{E2}$$

with the d-wave form factor g defined as

$$g(r) = \delta_{r_x,0}(\delta_{r_y,1}+\delta_{r_y,-1}) - \delta_{r_y,0}(\delta_{r_x,1}+\delta_{r_x,-1}) \tag{E3}$$

in Ref. [32]. This function is shown in Fig. 11. The long-range superconducting order is indicated by the saturation to a nonzero value around 0.055 at long distances.

[1] A. Damascelli, Z. Hussain, and Z.-X. Shen, *Angle-Resolved Photoemission Studies of the Cuprate Superconductors*, Rev. Mod. Phys. **75**, 473 (2003).

[2] D. Lu, I. M. Vishik, M. Yi, Y. Chen, R. G. Moore, and Z.-X. Shen, *Angle-Resolved Photoemission Studies of Quantum Materials*, Annu. Rev. Condens. Matter Phys. **3**, 129 (2012).

[3] M. Imada and Y. Hatsugai, *Numerical Studies on the Hubbard Model and the $t-J$ Model in One- and Two-Dimensions*, J. Phys. Soc. Jpn. **58**, 3752 (1989).

[4] E. Y. Loh, J. E. Gubernatis, R. T. Scalettar, S. R. White, D. J. Scalapino, and R. L. Sugar, *Sign Problem in the Numerical Simulation of Many-Electron Systems*, Phys. Rev. B **41**, 9301 (1990).

[5] N. Furukawa and M. Imada, *Optimization of Initial State Vector in the Ground State Algorithm of Lattice Fermion Simulations*, J. Phys. Soc. Jpn. **60**, 3669 (1991).

[6] M. Troyer and U.-J. Wiese, *Computational Complexity and Fundamental Limitations to Fermionic Quantum Monte Carlo Simulations*, Phys. Rev. Lett. **94**, 170201 (2005).

[7] E. Dagotto, *Correlated Electrons in High-Temperature Superconductors*, Rev. Mod. Phys. **66**, 763 (1994).

[8] C. Lanczos, *An Iteration Method for the Solution of the Eigenvalue Problem of Linear Differential and Integral Operators*, J. Res. Natl. Bur. Stand. **45**, 255 (1950).

[9] G. Vidal, *Efficient Simulation of One-Dimensional Quantum Many-Body Systems*, Phys. Rev. Lett. **93**, 040502 (2004).

[10] S. R. White and A. E. Feiguin, *Real-Time Evolution Using the Density Matrix Renormalization Group*, Phys. Rev. Lett. **93**, 076401 (2004).

[11] T. Maier, M. Jarrell, T. Pruschke, and J. Keller, *A Non-crossing Approximation for the Study of Intersite Correlations*, Eur. Phys. J. B **13**, 613 (2000).

[12] A. I. Lichtenstein and M. I. Katsnelson, *Antiferromagnetism and* ***d****-Wave Superconductivity in Cuprates: A Cluster Dynamical Mean-Field Theory*, Phys. Rev. B **62**, R9283 (2000).

[13] G. Kotliar, S. Y. Savrasov, G. Pálsson, and G. Biroli, *Cellular Dynamical Mean Field Approach to Strongly Correlated Systems*, Phys. Rev. Lett. **87**, 186401 (2001).

[14] T. D. Stanescu and G. Kotliar, *Fermi Arcs and Hidden Zeros of the Green Function in the Pseudogap State*, Phys. Rev. B **74**, 125110 (2006).

[15] G. Biroli, O. Parcollet, and G. Kotliar, *Cluster Dynamical Mean-Field Theories: Causality and Classical Limit*, Phys. Rev. B **69**, 205108 (2004).

[16] T. D. Stanescu, M. Civelli, K. Haule, and G. Kotliar, *A Cellular Dynamical Mean Field Theory Approach to Mottness*, Ann. Phys. Special Issue **321**, 1682 (2006).

[17] S. Sakai, G. Sangiovanni, M. Civelli, Y. Motome, K. Held, and M. Imada, *Cluster-Size Dependence in Cellular Dynamical Mean-Field Theory*, Phys. Rev. B **85**, 035102 (2012).

[18] M. Charlebois, D. Sénéchal, A.-M. Gagnon, and A. M. S. Tremblay, *Impurity-Induced Magnetic Moments on the Graphene-Lattice Hubbard Model: An Inhomogeneous Cluster Dynamical Mean-Field Theory Study*, Phys. Rev. B **91**, 035132 (2015).

[19] J. P. L. Faye and D. Sénéchal, *Interplay between d-Wave Superconductivity and a Bond-Density Wave in the One-Band Hubbard Model*, Phys. Rev. B **95**, 115127 (2017).

[20] S. Verret, J. Roy, A. Foley, M. Charlebois, D. Sénéchal, and A. M. S. Tremblay, *Intrinsic Cluster-Shaped Density Waves in Cellular Dynamical Mean-Field Theory*, Phys. Rev. B **100**, 224520 (2019).

[21] G. Carleo, F. Becca, L. Sanchez-Palencia, S. Sorella, and M. Fabrizio, *Light-Cone Effect and Supersonic Correlations in One- and Two-Dimensional Bosonic Superfluids*, Phys. Rev. A **89**, 031602(R) (2014).

[22] K. Ido, T. Ohgoe, and M. Imada, *Time-Dependent Many-Variable Variational Monte Carlo Method for Nonequilibrium Strongly Correlated Electron Systems*, Phys. Rev. B **92**, 245106 (2015).

[23] K. Ido, T. Ohgoe, and M. Imada, *Correlation-Induced Superconductivity Dynamically Stabilized and Enhanced by Laser Irradiation*, Sci. Adv. **3**, e1700718 (2017).

[24] T. Li and F. Yang, *Variational Study of the Neutron Resonance Mode in the Cuprate Superconductors*, Phys. Rev. B **81**, 214509 (2010).

[25] B. Dalla Piazza, M. Mourigal, N. B. Christensen, G. J. Nilsen, P. Tregenna-Piggott, T. G. Perring, M. Enderle, D. F. McMorrow, D. A. Ivanov, and H. M. Rønnow, *Fractional Excitations in the Square-Lattice Quantum Antiferromagnet*, Nat. Phys. **11**, 62 (2015).

[26] F. Ferrari and F. Becca, *Spectral Signatures of Fractionalization in the Frustrated Heisenberg Model on the Square Lattice*, Phys. Rev. B **98**, 100405(R) (2018).

[27] F. Ferrari, A. Parola, S. Sorella, and F. Becca, *Dynamical Structure Factor of the $J_1 - J_2$ Heisenberg Model in One Dimension: The Variational Monte Carlo Approach*, Phys. Rev. B **97**, 235103 (2018).

[28] K. Ido, M. Imada, and T. Misawa, *Charge Dynamics of Correlated Electrons: Variational Description with Inclusion of Composite Fermions*, Phys. Rev. B **101**, 075124 (2020).

[29] S. Yunoki, A. Moreo, E. Dagotto, S. Okamoto, S. S. Kancharla, and A. Fujimori, *Electron Doping of Cuprates via Interfaces with Manganites*, Phys. Rev. B **76**, 064532 (2007).

[30] F. Tan and Q.-H. Wang, *Two-Mode Variational Monte Carlo Study of Quasiparticle Excitations in Cuprate Superconductors*, Phys. Rev. Lett. **100**, 117004 (2008).

[31] A. S. Darmawan, Y. Nomura, Y. Yamaji, and M. Imada, *Stripe and Superconducting Order Competing in the Hubbard Model on a Square Lattice Studied by a Combined Variational Monte Carlo and Tensor Network Method*, Phys. Rev. B **98**, 205132 (2018).

[32] K. Ido, T. Ohgoe, and M. Imada, *Competition among Various Charge-Inhomogeneous States and d-Wave Superconducting State in Hubbard Models on Square Lattices*, Phys. Rev. B **97**, 045138 (2018).

[33] B.-X. Zheng, C.-M. Chung, P. Corboz, G. Ehlers, M.-P. Qin, R. M. Noack, H. Shi, S. R. White, S. Zhang, and G. K.-L. Chan, *Stripe Order in the Underdoped Region of the Two-Dimensional Hubbard Model*, Science **358**, 1155 (2017).

[34] See Supplemental Material at http://link.aps.org/supplemental/10.1103/PhysRevX.10.041023 for Source code of the code developed for this study and used in this article. The code is named "dVMC", is open-source and is a dynamical extension of code "mVMC" (Ref. [35]). Indications provided show how to compile and reproduce the results on Figs. 2(b), 3(b), 5(b), and 6(b) of the present article. Each of these figure should take under 20 min to calculate on 24 modern CPU.

[35] T. Misawa, S. Morita, K. Yoshimi, M. Kawamura, Y. Motoyama, K. Ido, T. Ohgoe, M. Imada, and T. Kato, *mVMC—Open-Source Software for Many-Variable Variational Monte Carlo Method*, Comput. Phys. Commun. **235**, 447 (2019).

[36] C. Moler and G. W. Stewart, *An Algorithm for Generalized Matrix Eigenvalue Problems*, SIAM J. Numer. Anal. **10**, 241 (1973).

[37] Note that the band Lanczos algorithm can also be reexpressed by this formalism. The main difference here is that we impose the translational symmetry from the beginning, and we do not orthogonalize at each iteration, aside from the variational form for the ground state. In fact, this technique is not iterative but is formulated in a chosen Krylov subspace. Nevertheless, this formalism would give the same result as the band Lanczos method, if the truncated Krylov subspace is systematically expanded.

[38] D. Tahara and M. Imada, *Variational Monte Carlo Method Combined with Quantum-Number Projection and Multi-Variable Optimization*, J. Phys. Soc. Jpn. **77**, 114701 (2008).

[39] S.-i. Amari, *Natural Gradient Works Efficiently in Learning*, Neural Comput. **10**, 251 (1998).

[40] S. Sorella, *Generalized Lanczos Algorithm for Variational Quantum Monte Carlo*, Phys. Rev. B **64**, 024512 (2001).

[41] R. Kaneko, S. Morita, and M. Imada, *Improved Multi-Variable Variational Monte Carlo Method Examined by High-Precision Calculations of One-Dimensional Hubbard Model*, J. Phys. Conf. Ser. **454**, 012046 (2013).

[42] M. Kawamura, K. Yoshimi, T. Misawa, Y. Yamaji, S. Todo, and N. Kawashima, *Quantum Lattice Model Solver* HΦ, Comput. Phys. Commun. **217**, 180 (2017).

[43] M. Capello, F. Becca, M. Fabrizio, S. Sorella, and E. Tosatti, *Variational Description of Mott Insulators*, Phys. Rev. Lett. **94**, 026406 (2005).

[44] C. Kim, A. Y. Matsuura, Z.-X. Shen, N. Motoyama, H. Eisaki, S. Uchida, T. Tohyama, and S. Maekawa, *Observation of Spin-Charge Separation in One-Dimensional* $\mathrm{SrCuO_2}$, Phys. Rev. Lett. **77**, 4054 (1996).

[45] C. Kim, Z.-X. Shen, N. Motoyama, H. Eisaki, S. Uchida, T. Tohyama, and S. Maekawa, *Separation of Spin and Charge Excitations in One-Dimensional* $\mathrm{SrCuO_2}$, Phys. Rev. B **56**, 15589 (1997).

[46] M. Kohno, *Spectral Properties near the Mott Transition in the One-Dimensional Hubbard Model*, Phys. Rev. Lett. **105**, 106402 (2010).

[47] M. Kohno, *Characteristics of the Mott Transition and Electronic States of High-Temperature Cuprate Superconductors from the Perspective of the Hubbard Model*, Rep. Prog. Phys. **81**, 042501 (2018).

[48] M. Kohno, *Mott Transition in the Two-Dimensional Hubbard Model*, Phys. Rev. Lett. **108**, 076401 (2012).

[49] E. A. Nowadnick, S. Johnston, B. Moritz, and T. P. Devereaux, *Renormalization of Spectra by Phase Competition in the Half-Filled Hubbard-Holstein Model*, Phys. Rev. B **91**, 165127 (2015).

[50] T. Ohgoe, M. Hirayama, T. Misawa, K. Ido, Y. Yamaji, and M. Imada, *Ab Initio Study of Superconductivity and Inhomogeneity in a Hg-Based Cuprate Superconductor*, Phys. Rev. B **101**, 045124 (2020).

[51] M. Imada and T. J. Suzuki, *Excitons and Dark Fermions as Origins of Mott Gap, Pseudogap and Superconductivity in Cuprate Superconductors—General Concept and Basic Formalism Based on Gap Physics*, J. Phys. Soc. Jpn. **88**, 024701 (2019).

[52] T. Misawa and M. Imada, *Origin of High-T_c Superconductivity in Doped Hubbard Models and Their Extensions: Roles of Uniform Charge Fluctuations*, Phys. Rev. B **90**, 115137 (2014).

[53] M. Soriano and J. J. Palacios, *Theory of Projections with Nonorthogonal Basis Sets: Partitioning Techniques and Effective Hamiltonians*, Phys. Rev. B **90**, 075128 (2014).